

Implosion dynamics and x-ray generation in small-diameter wire-array Z pinches

V. V. Ivanov, V. I. Sotnikov, J. M. Kindel, P. Hakel, R. C. Mancini, A. L. Astanovitskiy, A. Haboub, and S. D. Altemara
Department of Physics, University of Nevada, Reno, Nevada 89506, USA

A. P. Shevelko
Department of Physics and Astronomy, Brigham Young University, Provo, Utah 84602, USA
and P. N. Lebedev Physical Institute, Moscow 119991, Russia

E. D. Kazakov
P. N. Lebedev Physical Institute, Moscow 119991, Russia

P. V. Sasorov
Institute of Theoretical and Experimental Physics, Moscow 117259, Russia

(Received 26 September 2008; revised manuscript received 6 February 2009; published 21 May 2009)

It is known from experiments that the radiated x-ray energy appears to exceed the calculated implosion kinetic energy and Spitzer resistive heating [C. Deeney *et al.*, Phys. Rev. A **44**, 6762 (1991)] but possible mechanisms of the enhanced x-ray production are still being discussed. Enhanced plasma heating in small-diameter wire arrays with decreased calculated kinetic energy was investigated, and a review of experiments with cylindrical arrays of 1–16 mm in diameter on the 1 MA Zebra generator is presented in this paper. The implosion and x-ray generation in cylindrical wire arrays with different diameters were compared to find a transition from a regime where thermalization of the kinetic energy is the prevailing heating mechanism to regimes with other dominant mechanisms of plasma heating. Loads of 3–8 mm in diameter generate the highest x-ray power at the Zebra generator. The x-ray power falls in 1–2 mm loads which can be linked to the lower efficiency of plasma heating with the lack of kinetic energy. The electron temperature and density of the pinches also depend on the array diameter. In small-diameter arrays, 1–3 mm in diameter, ablating plasma accumulates in the inner volume much faster than in loads of 12–16 mm in diameter. Correlated bubblelike implosions were observed with multiframe shadowgraphy. Investigation of energy balance provides evidence for mechanisms of nonkinetic plasma heating in Z pinches. Formation and evolution of bright spots in Z pinches were studied with a time-gated pinhole camera. A comparison of x-ray images with shadowgrams shows that implosion bubbles can initiate bright spots in the pinch. Features of the implosions in small-diameter wire arrays are discussed to identify mechanisms of energy dissipation.

DOI: [10.1103/PhysRevE.79.056404](https://doi.org/10.1103/PhysRevE.79.056404)

PACS number(s): 52.59.Qy, 52.58.Lq

I. INTRODUCTION

Wire-array Z pinches are presently the most powerful laboratory source of x-ray radiation which [1–5] are applied for inertial confinement fusion (ICF) studies, radiation physics, laboratory astrophysics, and other areas of high-energy-density physics [6–8]. The impressive progress of Z pinches is linked to experiments at the 20 MA level of current but many aspects of complex Z pinch physics were studied at 1–3 MA generators [9–15]. It is well established that wire-array Z pinches pass through initiation, ablation, implosion, and stagnation phases [4,15]. The initiation stage is a predecessor of the ablation stage and can impact the formation of plasma flows in the Z pinch [16]. At the ablation stage wires stay at their initial positions because of the “core-corona” structure. In cylindrical wire arrays ablating material streams from the wires to the center of the array and forms a precursor plasma column [4,10,15]. The implosion phase starts when breaks arise on the wire cores and plasma “bubbles” are blown inward from the breaks. The plasma bubbles accelerate and snowplow material to the center of the array. The leading edges of the bubbles accrete ablated plasma, filling the array before the beginning of implosion stage and deliver plasma to the axis. The average radial speed of the

leading edge of imploding plasma was measured to be $(2-5) \times 10^7$ cm/s at the Zebra generator [14]. Bubblelike inhomogeneity of the imploding plasma seeds instabilities in the stagnating pinch [12–15] and also results in trailing mass [15,17]. Mitigation of plasma instabilities during the implosion phase in multiwire cylindrical, nested cylindrical, and starlike and planar wire arrays as well as multishell gas puffs provides enhanced power of the radiating x-ray pulse [1,2,18–20].

The study of physical mechanisms for energy deposition is crucial for understanding the x-ray production in Z pinches. It is known from experiments that the radiated x-ray energy can exceed the available implosion kinetic energy and Spitzer resistive heating [21–33]. Other mechanisms have been suggested to contribute in the Z pinch energy deposition [28–37]. These mechanisms include enhanced Ohmic heating due to anomalous resistivity caused by ion acoustic or lower hybrid turbulence [6] or the resistive effect in Hall plasma [32], dissipation of entrained magnetic flux [29–31], compressional work in the imploding plasma [28], interchange $m=0$ ion viscous heating [34], and $\mathbf{j} \times \mathbf{B}$ -forced expansion of the $m=1$ helix [35]. Plasma perturbations were also observed in the precursor of the wire arrays [38]. A theory of high beta electromagnetic flute-mode instabilities

could explain generation of perturbations and cells in the precursor [36].

An investigation of Z pinch energy balance provides evidence for enhanced plasma heating at the stagnation phase. The contribution of kinetic energy in cylindrical wire arrays depends on the convergence factor $\sim \ln(R_0/R_z)$ where R_0 and R_z are the initial radius of the array and the final radius of the stagnated Z pinch [6]. Recently, wire arrays with a 1 mm on-axis rod were tested in the 1 MA Z generator [39] to limit the convergence of the pinch. In these experiments the main radiation pulse can be explained by the $\mathbf{j} \times \mathbf{B}$ work. The bare-axis tests require submillimeter convergence of the magnetic field or enhanced plasma heating [39].

The mechanisms of the enhanced plasma heating have not been conclusively identified in previous experiments. In this paper any mechanisms of plasma heating with the exception of the kinetic-energy dissipation and Spitzer resistive heating in the homogeneous plasma column will be called “enhanced.” The contribution of kinetic energy can be minimized in the implosions of cylindrical wire arrays with small initial diameters. Diameter scaling from 6 to 80 mm and scaling of the wire number were carried out in cylindrical arrays [21–24,40–42] to optimize the power and energy of the x-ray pulse. An increase in the collapse velocity of Z pinches results in higher x-ray power and smaller diameter loads produced less x-ray yield. Cylindrical 6–8 mm loads were implemented by LePell and Jones for experiments on the Zebra generator [33]. These loads showed an enhanced soft x-ray yields compared to the 16 mm cylindrical wire arrays. Estimates show that the kinetic energy drops dramatically in cylindrical wire arrays of 1–2 mm in diameter if we suggest, based on x-ray pinhole images, that the final radius of the pinch is ~ 0.9 mm. Therefore implosions in cylindrical wire arrays with small diameters could indicate mechanisms of enhanced plasma heating in Z pinches.

In this paper, we present experimental investigations of implosions in wire arrays with high and low coupled kinetic energy. The implosion dynamics and x-ray production at the 1 MA Zebra generator were studied in cylindrical wire arrays from 16 to 1 mm in diameter and compared to a single-wire Z pinch. Loads of 3–8 mm in diameter generate the highest x-ray power at the Zebra generator. A fall of x-ray power in 1–2 mm loads can be linked to the less efficient nonkinetic mechanisms of plasma heating. In a small-diameter array the current-carrying plasma accumulates in the inner volume much faster than in loads of 12–16 mm in diameter. After the azimuthally correlated bubblelike implosion a significant part of the wire mass stays on the initial position at the beginning of the x-ray radiation. A time-gated x-ray pinhole camera shows different Z pinch dynamics in implosions with high and low kinetic energies. Wire arrays of 1–3 mm in diameter produce Z pinches with bright spots observed during the x-ray pulse generation. Long-lived and short-lived bright spots were observed in Al and W Z pinches. Shadowgraphy shows that implosion bubbles can initiate bright spots in the pinch. The electron temperature and density of Z pinches present a dependence on the load diameter similar to the dependence of radiated x-ray power and energy. Features of small-diameter wire-array implosions can help to identify mechanisms of energy dissipation in Z pinches.

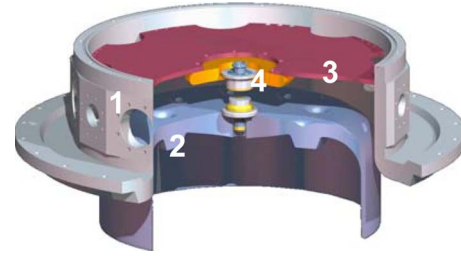


FIG. 1. (Color online) The setup of the Zebra vacuum chamber. (1) The chamber; (2) the high voltage cathode; (3) the anode plate; (4) the load installed on the axis between two adaptors. The diameter of the vacuum chamber is 60 cm.

II. EXPERIMENTAL SETUP

The experiments were carried out on the 1 MA Zebra generator at the Nevada Terawatt Facility [43]. Figure 1 explains the design of the vacuum chamber used in the experiments. Load (4) is installed on the axis of the vacuum chamber (1) between a couple of adaptors attached to the high voltage cathode (2) and the anode plate (3). In this configuration, the vacuum chamber wall serves as the current return path. This anode-cathode setup was used in all experiments. B dots for the current measurement are installed in the anode-cathode gap. The calculated inductance of the generator with a 16 mm load is 51 nH [44].

Optical plasma diagnostics on the Zebra generator included laser probing of the Z pinch in three directions, a streak camera, and a time-gated intensified charge-coupled device (CCD) [19,45,46]. The laser probing included two channels of shadowgraphy and a Faraday rotation channel. In two channels, pairs of delayed laser pulses propagated with orthogonal planes of polarization. In the third direction, the probing pulse was split after the vacuum chamber for the Faraday rotation diagnostic, shadowgraphy, and shearing interferometry. Magnetic fields in the wire arrays were estimated by the rotation of the polarization plane of the probing beam [45]. A short 150 ps laser pulse with a wavelength of 532 nm provided high-contrast images of the imploding plasma on CCD cameras. A long 34 ns train or a short 9 ns train of five laser probing pulses were available for probing. An optical streak camera with a slit was used to study the continuous implosion dynamics at a near-axial area of the wire arrays. A time-gated intensified CCD (ICCD) camera with a gate time of 3 ns was used to record the images of the radiating plasma. The streak camera and ICCD record radiation from a different direction than the direction of laser probing.

X-ray plasma diagnostics on the Zebra generator included filtered x-ray and photoconductive diodes, a bolometer, x-ray time-integrated and time-gated pinhole cameras, and spectrometers. The temporal profiles of the x-ray pulses were recorded with the x-ray diode (XRD) and photoconducting detectors (PCDs). The total radiated energy in the spectral region from 10 to 4–5 keV was measured with a bare Ni bolometer. The power of the x-ray pulse was calculated from the XRD filtered by 2 μm kimfol film normalized to the bare Ni bolometer yield. The time-gated pinhole camera re-

corded six frames with a spatial resolution of 0.25 mm in two spectral regions. The gate time of frames in experiments was 3 ns and the interframe delay was 10 ns. The x-ray spectra were recorded by a time-integrated spatial-resolved spectrometer with a convex KAP crystal [32]. The experiments were carried out with 2-cm-tall Al and W cylindrical wire arrays with masses of 30–200 $\mu\text{g}/\text{cm}$ and wire number of 8–32. Wire arrays with diameters 1, 2, 3, 5, 8, 12, and 16 mm and single-wire loads were tested in 49 shots on the Zebra generator. The implosions and x-ray yield in small-diameter wire arrays were compared with single-wire Z pinches.

III. IMPLOSIONS IN CYLINDRICAL ARRAYS OF 1–16 mm IN DIAMETER

Formation of the Z pinch in cylindrical loads with high kinetic energy has been well studied for currents up to 20 MA [4,5,39–42]. Implosion of small-diameter cylindrical loads, 1–3 mm in diameter, has not previously been intensively investigated. Comparison of the different types of loads showed that cylindrical arrays of 3 mm in diameter generate a high-power x-ray pulse with a short rising edge while the calculated kinetic energy decreases [18]. It was suggested that small-diameter wire arrays could clearly present nonkinetic mechanisms of plasma heating in Z pinches. In this section systematic studies of implosion dynamics, parameters of radiated x-ray pulses, and electron plasma temperature, and density are presented for cylindrical wire arrays with diameters from 1 to 16 mm.

A. Energy and power of the radiated x-ray pulse

Radiated x-ray power, energy, and plasma dynamics at the ablation, implosion, and stagnation phases were compared in cylindrical arrays with different diameters to find a transition from regimes dominated by kinetic-energy coupling to regimes with the lacking kinetic energy and with other prevailing mechanisms of plasma heating. The diameters of the wires were varied in cylindrical arrays to find the optimal masses for producing the maximum power and energy in the x-ray pulse. For example, in Al eight-wire 1 mm loads the wire diameter varied from 18 to 35 μm and in 16-wire 2–3 mm loads it varied from 10 to 25 μm . In W arrays the wire diameter varied from 4.3 to 12 μm .

Figure 2(a) presents the peak power of soft x-ray pulses radiated in implosions of Al cylindrical loads of 1–16 mm in diameter and in single-wire Z pinches. The power of the x-ray pulse was measured with the XRD filtered by the 2 μm kimfol filter. The plot presents the peak x-ray power as a function of wire-array masses for each load diameter. If a multipeak pulse was generated in the shot then the power of the highest peak was used for the diagram. The error bars present typical standard deviations of power and energy from the average value. Figures 2 and 3 represent data from 39 shots with Al loads. Shot-to-shot variation is the main source of errors in experiments on the Zebra generator. These variations arise due to small change in the current pulse, imperfections of loads, and electrical contacts.

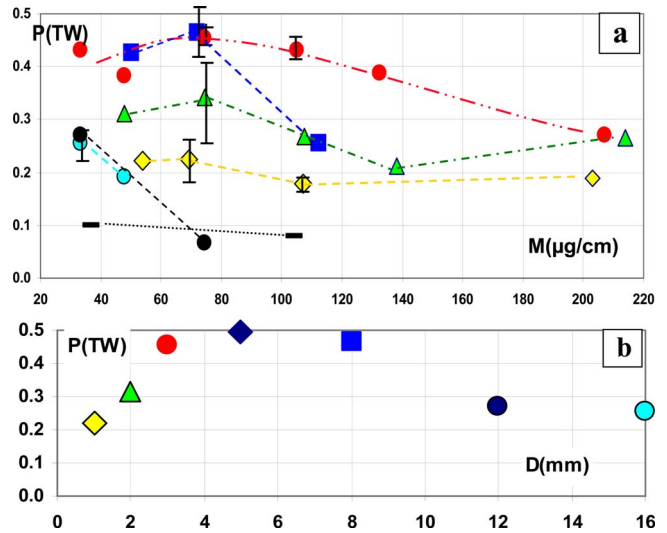


FIG. 2. (Color online) (a) The dependence of the soft x-ray power, calculated from the XRD with a 2 μm kimfol filter and Ni bolometer, on the mass in Al cylindrical wire arrays. It includes loads of 16 mm in diameter (light blue circles), 12 mm (dark blue squares), 8 mm (blue squares), 3 mm (red circles), 2 mm (green triangles), 1 mm (yellow diamonds), and single wire (rectangles). (b) The dependence of the maximum x-ray power of loads from diagram (a), with the same markers, on the diameter of the loads.

Cylindrical loads, 1–8 mm in diameter, generate the most x-ray power with masses of 30–80 $\mu\text{g}/\text{cm}$ (optimal masses). Single-wire loads generate the smallest x-ray power of ~ 0.1 TW that is less than in 1 mm wire arrays by a factor of 2. The maximum soft x-ray power of 0.4–0.45 TW is generated by loads of 3–8 mm in diameter. Figure 2(b) presents the maximum x-ray power generated in Al loads versus the initial load diameter. The radiated power falls in arrays of 12–16 mm in diameter and in arrays with a diameter of < 3 mm. The change in inductance between the 3 mm load and the arrays with diameters 16 and 1 mm is 6.7 and 4.4 nH, respectively. The measured maximum current in 1 mm loads is less by 3%–5% in comparison with the 3 mm loads. Small variations in the current cannot explain the fall of the x-ray power by 2–3 times but it can be linked to the fall of kinetic energy. The maximum current in the 16 mm loads was higher by 5%–8% in comparison with the 3 mm loads,

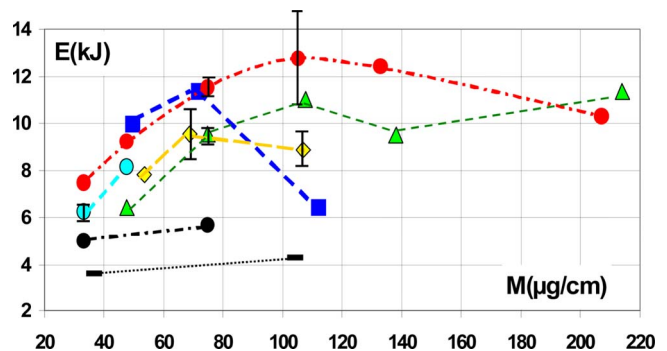


FIG. 3. (Color online) The dependence of the energy of the soft x-ray pulse on the masses of loads. Markers are the same as in Fig. 2.

but the radiated x-ray power dropped by ~ 2 times. The fall of the radiated power in large-diameter wire arrays can be linked to the high level of plasma instabilities and the inhomogeneous implosion. Large variations in the imploding front lead to spatial inhomogeneity and staggered arrival of the imploding plasma on the axis [14]. The wire cores are burnt out stochastically and the imploding plasma begins movement at different times. The imploding plasma bubbles from one wire can also have different speeds. The bubbles started first have enhanced speed and acceleration. Finally, the implosion on different wires begins at different times. The variation in bubble parameters leads to a distribution of material arriving on the axis, with a total delay of ~ 15 – 20 ns from the beginning to the end. The distribution of the material reaching the axis may be responsible for the long 15–25 ns rising edge of the x-ray pulse in 16 mm wire arrays. The x-ray power and pulse duration in Al of 12–16 mm cylindrical wire arrays depends on the interwire gap (IWG). This could indicate that ablation physics is important in these wire arrays [15,47]. Also, the dependence of the x-ray power pulse on the interwire gap in Al arrays has previously been studied in [40].

The radiated x-ray power also falls in wire arrays with very small diameters. This could be linked to the lack of kinetic energy in the imploding plasma and less efficiency of other mechanisms of plasma heating. A transition from the regime with high kinetic energy to the “nonkinetic” regime of plasma heating regime is observed in loads of < 3 mm in diameters.

Figure 3 presents the radiated x-ray energy in the same series of shots as in Fig. 2. Energy of the main x-ray pulse in the spectral range from 10 eV to 4 keV was measured with a Ni bolometer. The total XRD pulse was normalized to the bolometer yield. This calibration was used for the calculation of the x-ray energy radiated in the prepulse, rising edge, and main pulse. The energy diagram presents trends similar to the power diagram but optimal masses for radiated energy are higher, 70–110 $\mu\text{g}/\text{cm}$ in wire arrays of 1–8 mm in diameter. The fall of total radiated energy in 1–2 mm loads is smaller than the fall of power. These loads radiate high x-ray energy because the fall of power is compensated by the longer pulse duration. Aluminum wire arrays with diameters of 1–8 mm produce an x-ray energy of 11–13 kJ. Aluminum single wires generate soft x-ray energy of ~ 4 kJ in a long 200–240 ns pulse.

Due to the limitation for the acceptable load mass in the Zebra generator, cylindrical arrays with different wire-numbers and IWG are presented in Figs. 2 and 3. The value of the IWG impacts the x-ray production in large-diameter cylindrical loads in multi-MA generators [1,22,23,40]. The impact of the IWG on implosions of small-diameter Al loads in the Zebra generator was tested in a series of shots. Figures 4(a) and 4(b) present the radiated x-ray power and energy in Al 3 mm cylindrical arrays with wire numbers from 4 to 24 (IWG=0.4–2.4 mm). In loads with similar masses, the variation in power is about the shot-to-shot variations. The diagram of the total radiated energy, Fig. 4(b), also does not show a significant dependence of radiated energy on the IWG.

The delays from the peak of the x-ray pulse to the beginning of the current pulse are presented in Fig. 5. In multipeak

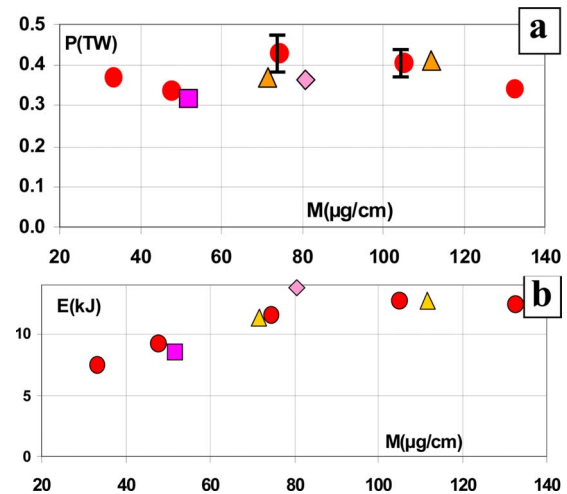


FIG. 4. (Color online) The dependence of the (a) soft x-ray power and (b) energy on the mass in Al cylindrical wire arrays 3 mm in diameter, including loads with IWG=2.4 mm (squares), IWG=0.8 mm (diamonds), IWG=0.6 mm (circles), and IWG=0.4 mm (triangles).

pulses the delay to the first significant peak ($> 50\%$ of the maximum) was measured. The diagram shows a strong dependence of the implosion time on the load mass for wire arrays 12–16 mm in diameter. Due to the large time of flight of imploding plasma, large-diameter overmassed loads implode after the maximum of the current pulse and demonstrate a fall of radiated energy and power. This dependence is smaller for loads of 1–3 mm in diameter. In 1 mm loads with an optimal mass the first peak of the x-ray pulse arises on the rising edge of the current pulse at the level 40%–50% of the maximum current.

X-ray power and yield in tungsten cylindrical wire arrays with diameters 1, 2, 3, and 8 mm were also studied. Tungsten loads with diameter of 3 and 8 mm produced the highest power in this series. Radiated power decreases in W 2 and 1 mm loads as it was measured in Al loads. This supports the suggestion about the change in the regime of plasma heating in small-diameter wire-array Z pinches.

B. Implosion and stagnation dynamics

Ablation and stagnation phases in cylindrical wire arrays with high kinetic energy have been well investigated [4]. At

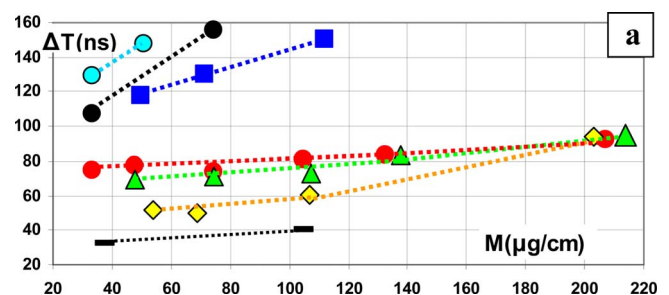


FIG. 5. (Color online) The delay from the beginning of the current pulse to the peak of the x-ray pulse in cylindrical wire arrays with different diameters and masses. Loads with different diameters are marked similar to Figs. 2 and 3.

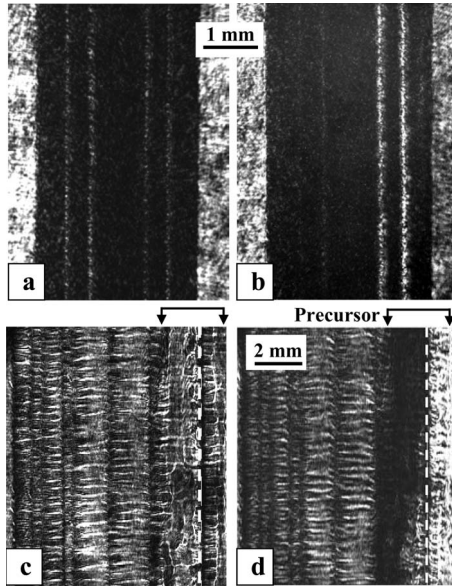


FIG. 6. [(a),(c) and (b),(d)] The shadowgrams and the complementary Faraday images in Al wire arrays. [(a) and (b)] Shot 1150, a 16-wire 3 mm in diameter load with a mass of $75 \mu\text{g}/\text{cm}$; [(c) and (d)] Shot 662, a 24-wire 16 mm in diameter load with a mass of $50 \mu\text{g}/\text{cm}$. The timing of frames (a),(b) and (c),(d) to the beginning of the current pulse is 39 and 82 ns. The initial angle of rotation is $\alpha_0=5^\circ$.

the ablation stage, the $\mathbf{j} \times \mathbf{B}$ force moves the “corona” plasma to the center of the array. According to the rocket model the rate of mass ablation per unit length, dm/dt is [15]

$$\frac{dm}{dt} = \frac{\mu I^2}{4\pi V_{abl} R_0}, \quad (1)$$

where I is the drive current, R_0 is the initial radius of the array, and V_{abl} is the velocity of the ablating plasma. The ablation rate is $\sim 1/R$ and increases in small-diameter loads. The inner volume V of the cylindrical load depends on the radius R such that $V \sim R^2$. For example, the accumulation of plasma in the volume of the 2 mm load could be faster by ~ 500 times compared to the 16 mm load. The ablation rate V_{abl} can vary with the variation in some load parameters [15] but the strong dependence on the radius dominates in this case.

Experiments on the Zebra generator show that small-diameter wire arrays become opaque for optical laser probing in the ablation phase. Shadowgraphy shows a precursor formation at the beginning of the ablation stage when the load is transparent for laser probing. The precursor diameter is < 1 mm in the 3 mm load which is less than in the 12–16 mm loads [45,46]. The shadowgram and Faraday image in Figs. 6(a) and 6(b) present a moment at a delay of 36 ns and 33% of the current maximum. In Fig. 6(a) only the narrow interwire areas are transparent for probing light at a wavelength of 532 nm. Comparison of (a) the shadowgram with (b) the Faraday image shows magnetic fields in the ablating plasma. Darkening of the left side and lightening of the right side of the load are seen in the Faraday image compared to the shadowgram. The magnetic fields on the left side have

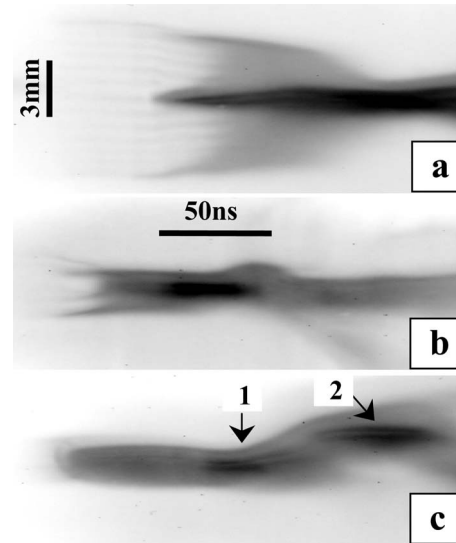


FIG. 7. Streak images of implosions in cylindrical wire arrays. (a) Shot 1233 with a 32-wire 8 mm in diameter load with a mass of $66 \mu\text{g}/\text{cm}$. (b) Shot 1234 with a four-wire 3 mm in diameter load, $52 \mu\text{g}/\text{cm}$. (c) Shot 1230 with a 16-wire 2 mm in diameter load, $48 \mu\text{g}/\text{cm}$.

opposite directions compared to the right sides of the array; therefore current flows in the ablating plasma (see details in [45]). For comparison, a shadowgram and Faraday image in 16 mm 24 wire loads are presented in Figs. 6(c) and 6(d). The Faraday rotation of the polarization plane of the probing beam produces lightening and darkening in right and left sides of the precursor. The current value in the precursor is $\sim 10\%$ of the total current estimated in 16 mm loads [45]. The current in the plasma filling the wire array could be a driving force for plasma instabilities.

The implosion phase starts when breaks arise on the wires and the main portion of the material begins moving to the center of the array. The implosion stage was studied by the optical streak camera and five-frame shadowgraphy. Figure 7(a) presents a typical implosion dynamics in cylindrical loads of 8–16 mm in diameter. A streak image shows radiation from wires at the ablation phase, the formation of the precursor, the implosion of wires, and the stagnation of the pinch. Optical streak images of implosions in small-diameter loads are presented in Figs. 7(b) and 7(c). Arrow (1) points to the bright area in the center of the array which is timed to the radiated x-ray pulse. The radial size of the array does not change significantly during the implosion and stagnation phases. This indicates that a significant part of wire material is staying on the initial position of the wires. The fine structure and instabilities in the imploding pinch are not resolved on the streak camera but they are seen in the shadowgrams presented below. The Z pinch produced by the small-diameter loads [Figs. 7(b) and 7(c)] stagnates for a longer time period than the pinch in the large-diameter arrays [Fig. 7(a)]. Arrow (2) in Fig. 7(c) points to the second bright area during the stagnation phase in the 1 mm wire-array Z pinch.

Multiframe shadowgraphy shows two-dimensional (2D) features of implosion and stagnation phases in small-diameter wire arrays. In Figs. 8(a)–8(d) central areas of wire

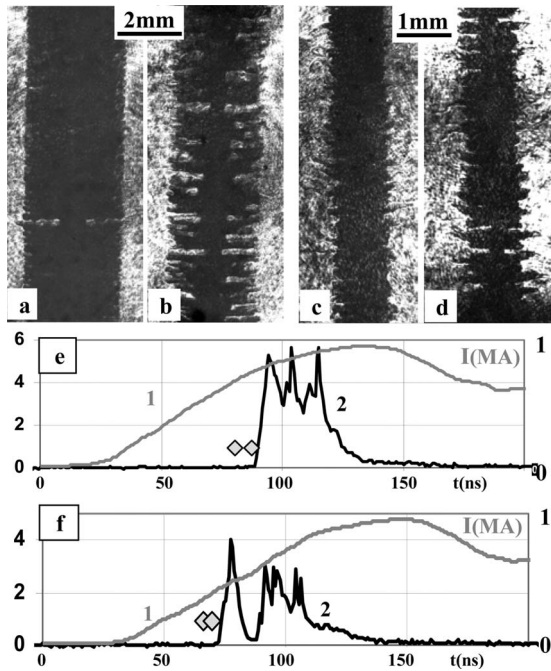


FIG. 8. Two pairs of shadowgrams (a),(b) and (c),(d) and timing diagrams (e) and (f) from two shots, [(a), (b), and (e)]1059 and [(c), (d), and (f)] 1173. Frames (a) and (b) present the implosion in the Al 16-wire 3 mm in diameter load, $105 \mu\text{g}/\text{cm}$, with 7 ns between frames. Frames (c) and (d) present the implosion in the Al eight-wire load of 1 mm in diameter, $104 \mu\text{g}/\text{cm}$, with 4.2 ns between frames. Line (1) in timing diagrams presents the current pulses, line (2) is the x-ray pulses from the PCD with a Be $8 \mu\text{m}$ filter, and the diamonds show positions of laser frames.

arrays present the implosion dynamics. Images (a) and (b) present two frames of the shadowgraphy from the 3 mm load recorded from the same probing direction, with 7 ns between frames. It is seen in Fig. 8 that the imploded material in 1–3 mm loads is pushed by plasma bubbles similar to the large-diameter arrays [14]. Axial positions of bubbles from different wires are azimuthally correlated. The correlation of breaks on the wire was also observed in large-diameter wire arrays [17,48]. A high degree of the azimuthal correlation in small-diameter loads could be linked to the large global magnetic field. During the implosion, correlated bubbles produce “necks” with diameters of 0.5–0.7 mm on the stagnated Z pinch. A stagnating pinch is initially axially modulated by implosion bubbles. The period of the axial modulation approximately matches the fundamental ablating period in Al wire arrays [15,19]. A significant part of the wire-array material stays at the initial position of wires during the generation of the main x-ray pulse. The timing diagram in Fig. 8 indicates that frame (b) is recorded 5 ns before the beginning of the x-ray pulse. In the 1 mm load [see Figs. 8(c) and 8(d)] the implosion dynamics are similar to implosion dynamics in the 3 mm load. Two frames of shadowgraphy with 4.2 ns between them present a bubblelike implosion with the axial period of ~ 0.4 mm. In shadowgrams the diameter of the pinch in the necking region is 0.25–0.5 mm. The delay of frame (d) to the beginning of the x-ray pulse is ~ 5 ns.

The implosion dynamics in W wire arrays are similar to Al loads. Figure 9 presents a four-frame shadowgram of the

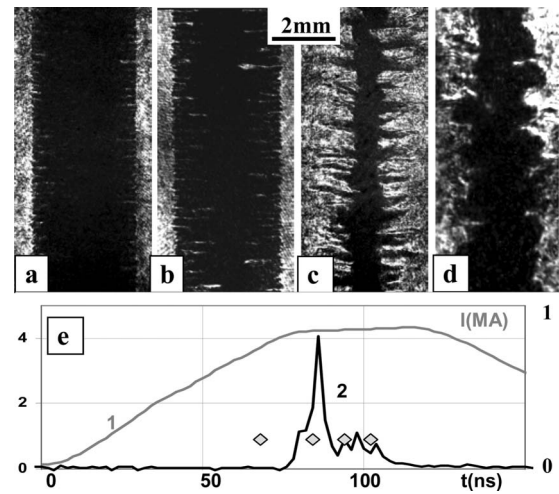


FIG. 9. [(a)–(d)] The four-frame shadowgram from shot 1418 with a W 16-wire load 3 mm in diameter, with a mass of $141 \mu\text{g}/\text{cm}$. The timing diagram (e) presents the current pulse (1), the x-ray pulse (2), and the frames of shadowgraphy (diamonds).

Z pinch evolution in the W 16-wire cylindrical load of 3 mm in diameter. The development of the Z pinch was recorded in one shot with a 34 ns train of five probing pulses. Figure 9(a) presents the beginning of the bubblelike implosion. The axial period of bubbles is less than in Al loads because the fundamental period of ablation is ~ 0.25 mm in W wire arrays [19,46]. A bubblelike implosion produces a Z pinch seen in Figs. 9(b) and 9(c). In Fig. 9(d) the pinch begins to expand. Later, the structure of the pinch is similar to the structure of the single-wire Z pinches, with necks, “bulges,” and “flares” [49–51] signifying the growth of an $m=0$ magnetohydrodynamics (MHD) instability. Nevertheless, 1 mm wire-array Z pinches produce significantly more power and energy compared to the single-wire Z pinch. The single-wire Z pinch passes through the stage with a core-corona structure [51]. The single wire radiates x rays from the beginning of current pulse, Fig. 10(e). In wire arrays, the imploding plasma forms a Z pinch. This pinch exists only after the implosion of the array. The large difference between the radiated x-ray pulses is a result of the different pinch histories which lead to different plasma conditions in Z pinch plasmas.

Important information about the implosion and stagnation phases is delivered by XRDs and PCDs filtered for different spectral ranges. Figure 10 presents the shape and duration of soft x-ray pulses generated by cylindrical wire arrays of (a)–(d) 16, 8, 2, and 1 mm in diameter and by the single-wire Z pinch (e). Shaded areas and some features in figure (d) will be explained below in Sec. IV. Wire arrays of 12–16 mm in diameter generate a 25–35 ns x-ray pulse with a long prepulse and tail, Fig. 10(a). Loads of 5–8 mm in diameter radiate the highest x-ray power with the pulse duration of 16–20 ns. A tail after the main x-ray pulse is typical for loads with mass $>70 \mu\text{g}/\text{cm}$. A prepulse in cylindrical arrays is generated by the precursor. In 2–3 mm loads the x-ray pulses become wider but have steep 5–8 ns rising edges, Fig. 10(c). The x-ray pulse from the 1 mm array has a pulse duration of ~ 50 ns and a multipeak structure, Fig. 10(d). Optical diagnostics show that the first x-ray peak correlates with the

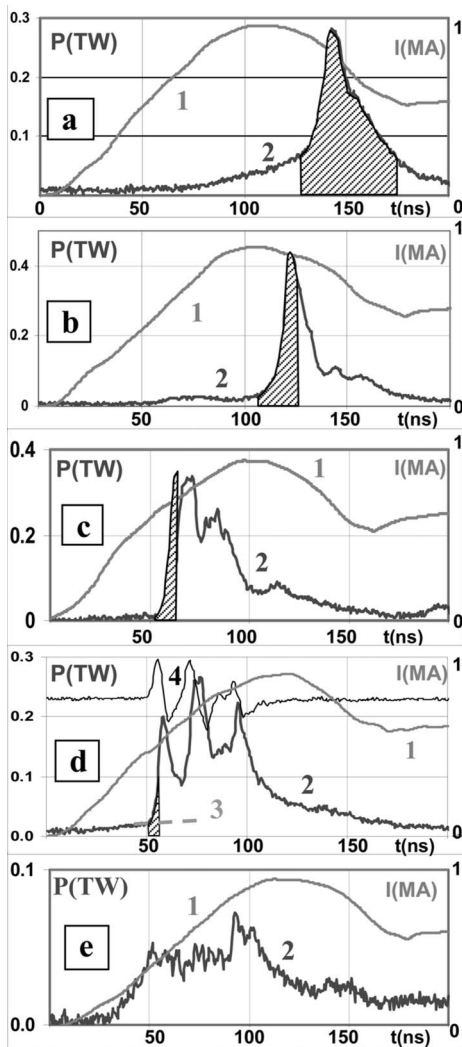


FIG. 10. The x-ray pulses generated in Al cylindrical loads with diameters of 16 mm, $33 \mu\text{g}/\text{cm}$ (a), 8 mm, $50 \mu\text{g}/\text{cm}$ (b), 2 mm, $75 \mu\text{g}/\text{cm}$ (c), 1 mm, $69 \mu\text{g}/\text{cm}$ (d), and single wire of $70 \mu\text{m}$ in diameter, $102 \mu\text{g}/\text{cm}$ (e) Line (1) presents the current pulse and line (2) is the x-ray pulse from the XRD filtered by a $2 \mu\text{m}$ kimfol filter normalized to the bolometer yield. Shaded areas show the calculated kinetic energy with the final pinch diameter of 0.9 mm (see Sec. IV for details). Line (3) in image (d) is the calculated power of the Spitzer heating and line (4) is the derivative of the x-ray pulse (2). Line 4 shows the derivative dP/dt of the x-ray pulse.

bubblelike implosion. Other peaks in the x-ray pulse could be linked to the features of plasma heating or the additional implosions in small-diameter wire arrays. For comparison, the x-ray pulse from a single-wire Z pinch is presented in Fig. 10(e). The duration of the soft x-ray pulse in this diagram is comparable with the duration of the current pulse. The power of keV x-ray radiation falls in small-diameter wire arrays. Nevertheless, 1–2 mm loads produce keV x-ray pulses with a power of $\sim 40\text{--}50\%$ of the keV x-ray pulses generated by 5–8 mm loads.

While diagrams in Fig. 2 show a fall of the radiated x-ray power in 1–2 mm loads, a time-gated pinhole camera indicates a different radiative structure and Z pinch dynamics in

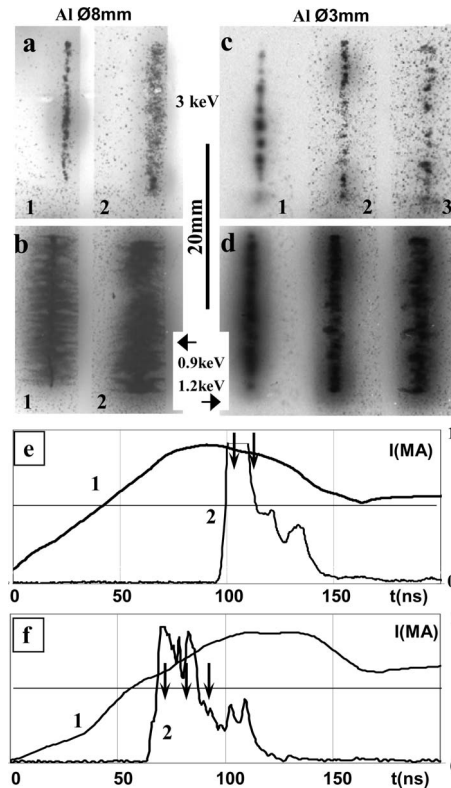


FIG. 11. X-ray images from the time-gated pinhole camera [(a)–(d)] and timing diagrams [(e)–(f)]. [(a), (b), and (e)] Two frames from shot 1002 with a 24-wire Al load 8 mm in diameter, $50 \mu\text{g}/\text{cm}$. [(c), (d), and (f)] Three frames from shot 1229 with a 16-wire Al load of 3 mm in diameter, $33 \mu\text{g}/\text{cm}$. The anode is on the top of the images. The images are filtered by a $15 \mu\text{m}$ Be foil (b), $25 \mu\text{m}$ Be foil (d), $15 \mu\text{m}$ Be foil and $110 \mu\text{m}$ Mylar film (a), $15 \mu\text{m}$ Be foil and $110 \mu\text{m}$ Mylar film (c). Line (1) in the timing diagram presents the current pulse, line (2) is the x-ray pulse from the PCD, and the arrows show the positions of 3 ns frames (with 10 ns between frames).

large- and small-diameter wire arrays. Figures 11(a)–11(d) present x-ray images of radiating Z pinches in 3 ns frames with 10 ns between frames from the [(a) and (b)] 8 mm load and [(c) and (d)] 3 mm wire array. Frames (b) and (d) are filtered for energies $E > 0.9$ and > 1.2 keV, respectively (for the 10% transmission coefficient), and present Al K-shell radiation from plasma columns of 3–4 mm in diameter. These columns could consist of the trailing mass (in the 8 mm load) and material staying at the initial position of the wires (in the 3 mm load). The pinch is seen on the axis of the plasma column. Frames (a) and (c) are filtered for $E > 3$ keV and show the Z pinch in harder x-ray radiation. Frame (a1) shows the formation of the pinch ~ 1 mm in diameter in 8 mm wire array. Frame (a2), 10 ns later, shows the radial expansion of the radiating area with a radial velocity of $\sim 10^7$ cm/s. Small-diameter wire-array Z pinch evolves another way and the stagnating pinch exists for a longer time. The stagnating Z pinch in frames (c1)–(c3) includes a chain of bright radiating regions of 0.5–1 mm in diameter. These spots arise near the maximum of the x-ray pulse and exist > 30 ns during the main x-ray pulse. Periodic structure of the pinch is typical

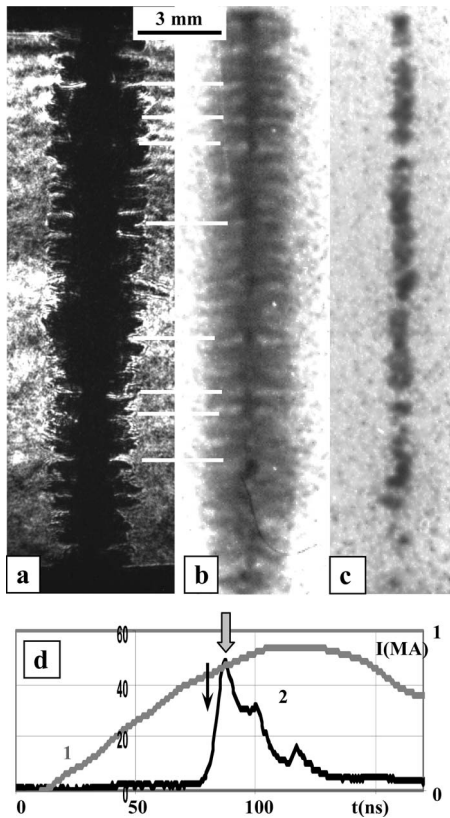


FIG. 12. (a) The shadowgram, [(b) and (c)] the x-ray images from the time-gated pinhole camera, and (d) the timing diagram in shot 1003 with a 16-wire load 3 mm in diameter, $75 \mu\text{g}/\text{cm}$. Image (b) is filtered for $E > 0.9 \text{ keV}$ and image (c) is filtered for $E > 3 \text{ keV}$. Narrow and wide arrows show the timing of the shadowgram and x-ray frames. The anode is on the top of the images.

for implosions in small-diameter wire arrays. The period of spots exceeds the fundamental frequency, presumably, because of the axial merging of bubbles during implosion. The axial positions of bright spots correlate with the positions of implosion bubbles. Figures 12(a)–12(c) compares a shadowgram (a) with time-gated x-ray images [(b) and (c)] at the end of the implosion phase. The images in Fig. 12 are aligned axially using the positions of electrodes and magnification of the cameras. The structure of the imploded wire array in x-ray image (b), $E > 0.9 \text{ keV}$, is similar to the shadowgram (a). This leads to the suggestion about the initiation role of bubbles in the formation of necks and primary bright spots in the Z pinch. The necks in the shadowgram and self-radiation x-ray image are partly correlated. Some of the necks in the shadowgrams are hidden by the nonimploded plasma which is nontransparent to the laser radiation at 532 nm. The nonimploded plasma can also hide necks in x-ray images. The shadowgram shows a 7 ns earlier time compared to the x-ray image and parts of the necks are still not formed. The correlation of bright spots with “swept areas” on the trailing material was also observed in large-diameter cylindrical wire arrays [52]. In low wire-number arrays swept areas are produced by implosion bubbles [14]. Bright spots in an x-ray image (c), $E > 3 \text{ keV}$, mostly follow the axial positions of necks in image (b). Nevertheless, some necks in

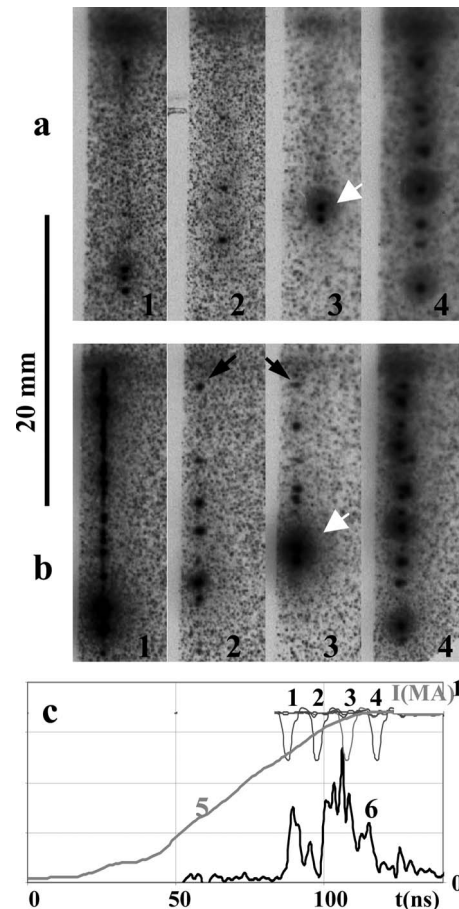


FIG. 13. [(a) and (b)] Four frames from the x-ray pinhole camera and (c) the timing diagram from shot 1424 with a W eight-wire load 3 mm in diameter, $175 \mu\text{g}/\text{cm}$. [(a) and (b)] The anode is on the top of images. Lines (1)–(4) in the diagram present the timing of frames (1)–(4), line (5) is the current pulse, and line (6) is the x-ray pulse from the PCD with a $8 \mu\text{m}$ Be filter. Images in (a) are filtered for $E > 3 \text{ keV}$ and images in (b) are filtered for $E > 1.2 \text{ keV}$.

the keV image (b) do not produce bright spots in 3 keV x-ray image (c). Some spots in the keV range are seen in several frames for 20–30 ns. These spots can arise, fade, and become brighter again during the main x-ray pulse. Some of the bright spots do not have pronounced predecessors in previous frames and arise at the stagnation stage. The identification of spots in x-ray images was limited in our experiments by the spatial resolution of the time-gated pinhole camera, $\sim 0.2 \text{ mm}$. Note that bright spots are observed in vacuum sparks, X pinches, and Z pinches [53–55].

Bright spots of another type were observed in W loads. Figure 13 presents the evolution of bright spots in a W 1 mm eight-wire array. Row of frames (a) presents the x-ray images in the range $E > 3 \text{ keV}$ and row of frames (b) present images with $E > 1.2 \text{ keV}$. The delay between frames (1) and (4) is 10 ns with a frame duration of $\sim 3 \text{ ns}$. White arrows point to the powerful x-ray burst in both 0.9 and 3 keV images. This burst does not have predecessors and successors in other frames. It exists for a short time and correlates with a short nanosecond spike in the XRD pulse in Fig. 13(c), frame (3). A chain of bright spots arises in frame (4). Some spots in

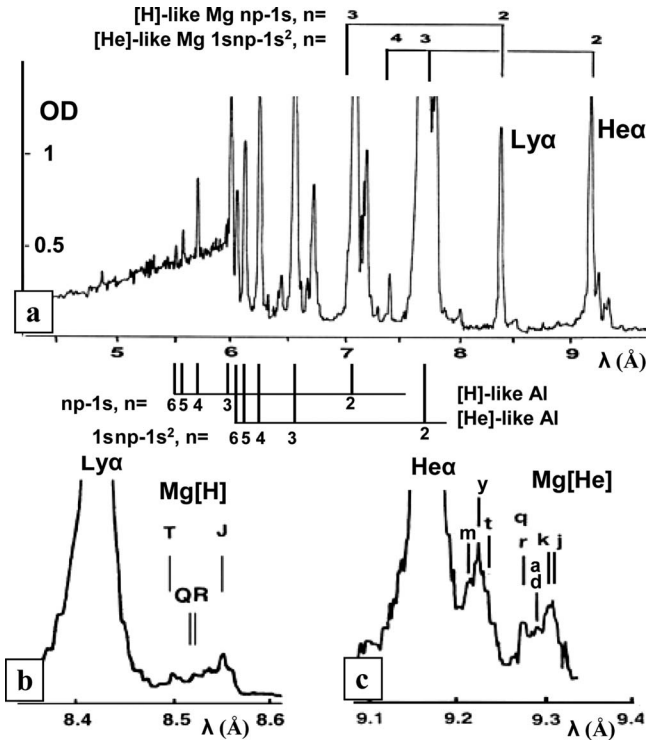


FIG. 14. (a) The x-ray spectrum from the Al (5056 alloy with 5% Mg) Z pinch; magnified parts of spectra with (b) H-like and (c) He-like satellites.

frame (b4) have predecessors in frame (b3), and other spots do not have it. Bright spots in the range >3 keV typically do not have predecessors and successors and live for a short time.

C. Electron temperature and density of Z pinch plasma

The electron temperature and density of Z pinch plasmas were extracted from the analysis of time-integrated x-ray line spectra. Spectra of H- and He-like Mg and Al ions were recorded by an x-ray spectrometer with a convex KAP crystal 50 mm in radius [56] on BIOMAX-MS film [57]. A spectral resolution of $\lambda/\delta\lambda \sim 350$ was derived from the width of the isolated lines and also calculated for the source with a radial size of 1 mm. A 0.5 mm slit provided an axial spatial resolution of ~ 1.5 mm. The spectral range of observation was $\lambda=5-10$ Å. The aluminum alloy 5056 used in wire arrays includes 5% of Mg. The photon energy range of the spectrometer was adequate to record K-shell lines of H- and He-like Al and Mg ions. Lyman series lines $np-1s$ in H-like Mg and Al ions and $1snp-1s^2$ lines in He-like Mg and Al ions were observed in the spectra, see Fig. 14(a), including satellite line transitions arising from autoionizing states in Li- and He-like ions near 2–1 and 3–1 transitions in H- and He-like ions [Figs. 14(b) and 14(c)]. A calibrated film scanner and Joice-Loyble microdensitometer were used for film scanning. Optical density was converted to intensity scale using the film calibration curve. Mg lines were selected for diagnostics because Mg H- and He-like resonance lines are isolated (i.e., do not overlap with Al lines) and the concen-

tration of Mg in the alloy is ~ 20 times smaller than that of Al. The small concentration of Mg in the Z pinch plasma helps to reduce the impact of opacity on spectral measurements. The opacity for a Doppler-broadened line can be estimated by the formula [58]

$$\tau = 3.52 \times 10^{-13} f_{nm} \lambda (Mc^2/kT)^{1/2} NL = 5.4 \times 10^{-9} f_{nm} \lambda (\mu/T)^{1/2} NL, \quad (2)$$

where f_{nm} is the absorption oscillator strength, λ is the wavelength, and L is the physical depth of the plasma; M , N , and T are the mass, number density (all in cgs units), and the temperature of the absorber in eV; μ is M divided by the proton mass. For a line to undergo moderate radiation transport effects (i.e., quasioptically thin) then $\tau < 1$. In our case $\lambda = 9 \times 10^{-8}$ cm, $\mu = 24$, $T = 400$ eV [18], the radius of the pinch is $L = 0.05$ cm, $Z = 12$, and $N_i = 10^{20}$ cm $^{-3}/Z$. If we take into account the 5% concentration of Mg and, for the sake of estimation, assume an equal distribution between H- and He-like ions in the Z pinch plasma and $f_{nm} = 0.4-0.8$ for H- and He-like resonance lines, then $\tau = 0.5-1$. However, in the same plasma $\tau = 10-20$ for Al H- and He-like resonance lines. This estimate shows that Mg lines have acceptably low levels of opacity in these experiments.

Resonance lines $Ly\alpha$, $He\alpha$, and their associated satellites were used for diagnostics of plasma parameters [59–61]. Satellites J of Mg H-like $Ly\alpha$ and $j+k$ of Mg He-like $He\alpha$ resonance lines were used to estimate the electron plasma temperature T_e . These satellites are dielectronic in comparison with more collisionally driven (inner-shell) q and a , d , and r satellites. All satellites of H-like lines including the J satellite are dielectronic ones. The satellite structures in H- and He-like Mg spectra are labeled according to the notation of Gabriel [62]. On one hand, the resonance $He\alpha$ and intercombination y lines of He-like ions, $k+j$ dielectronic satellites, $Ly\alpha$ resonance line of H-like ions, and dielectronic satellite are resolved. On the other hand, with a resolving power of $\lambda/\delta\lambda \sim 350$, j and k satellites are not separated and we used the sum $j+k$; but satellite J and the pair $j+k$ are well separated from the resonance lines and other satellites. Satellite J is resolved from the most intense collisionally excited satellite q . Satellites a , d , and r could give only a small contribution to the measured intensity of $j+k$. Resonance lines and corresponding dielectronic satellites are excited from the same level in ionization stages of H- or He-like ions and changes in ionization distribution alone do not impact the relative intensity of the resonance and satellite lines. Moreover, resonance lines and nearby satellites spread over a narrow spectral band, and thus they are less sensitive to the details of the spectral calibration of the spectrometer. This method does not include any free parameters and is convenient for the comparison of T_e and N_e in different types of wire arrays.

Using the intensity ratio of resonance line $Ly\alpha$ of H-like ions to dielectronic satellite J , the electron temperature T_e [H] was derived. The electron temperature T_e [He] was calculated from the intensity ratio of the resonance line $He\alpha$ to dielectronic satellites $j+k$. The electron density N_e extracted the intensity ratio of the resonance line $He\alpha$ to the intercom-

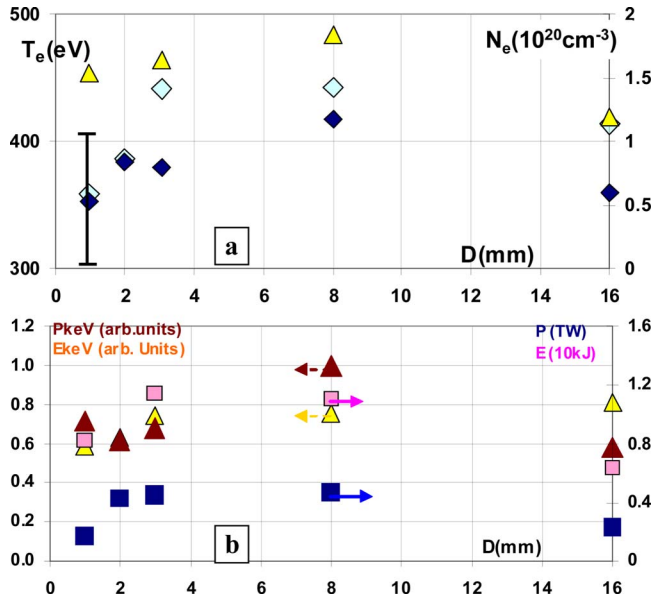


FIG. 15. (Color online) (a) The dependence of T_e [H] (light diamonds), T_e [He] (dark diamonds), and N_e (triangles) on the diameters of cylindrical wire arrays. (b) The dependence of the total (squares, right axis) and keV (triangles, left axis) radiated x-ray power and energy on the diameters of loads. Dark markers present the power and light markers show the energy.

bination γ line in He-like ions [59]. An additional channel for population of $2p$ levels was taken into account due to the mixture of $2s$ and $2p$ levels in H- and He-like ions. Collisional mixture of $2s$ and $2p$ levels for H- and He-like Mg ions begins at $N_e \geq 10^{16} \text{ cm}^{-3}$ [61]. This correction to the resonance line intensities leads to $\sim 10\%$ correction for T_e .

Axial inhomogeneity of the pinch is seen in axially resolved spectra. The spectra include dark and light regions at certain axial positions in the pinch. The axial resolution of the spectrometer with a 0.5 mm slit is 1.5 mm and the small-size bright spots are not resolved in the spectra. The spectra from dark areas were processed, suggesting that these areas with the enhanced energy of the x-ray radiation represent the majority of the radiated K -shell energy. Figure 15(a) shows the dependence of T_e and N_e in the Z pinch plasma on the initial diameters of the wire arrays. The accuracy of measurements is $\pm 10\%$ for the electron temperature T_e and $\pm 25\%$ for the electron density N_e . The triangles in Fig. 15(a) present the density N_e and the diamonds show the electron temperature T_e [He] (dark diamonds) and T_e [H] (light diamonds). For comparison, the x-ray energy and power radiated by these loads are presented in Fig. 15(b). The total (mostly, soft) radiated x-ray energy E and power P are marked by squares. The keV-range energy E_k and power P_k are marked by triangles. The energy and power in both x-ray ranges show similar trends. The radiated energy and power fall in 16 and 1–2 mm loads and in the single-wire Z pinch. Figure 15(a) shows a decrease in the electron temperature T_e in loads with diameter 16 and 1 mm.

A coronal equilibrium (CE) model was used in [59] to calculate the dependence of T_e on the intensity ratio of dielectronic satellites and resonance lines. The CE model is valid up to the electron density N_e of $\sim 4 \times 10^{18} \text{ cm}^{-3}$ [63].

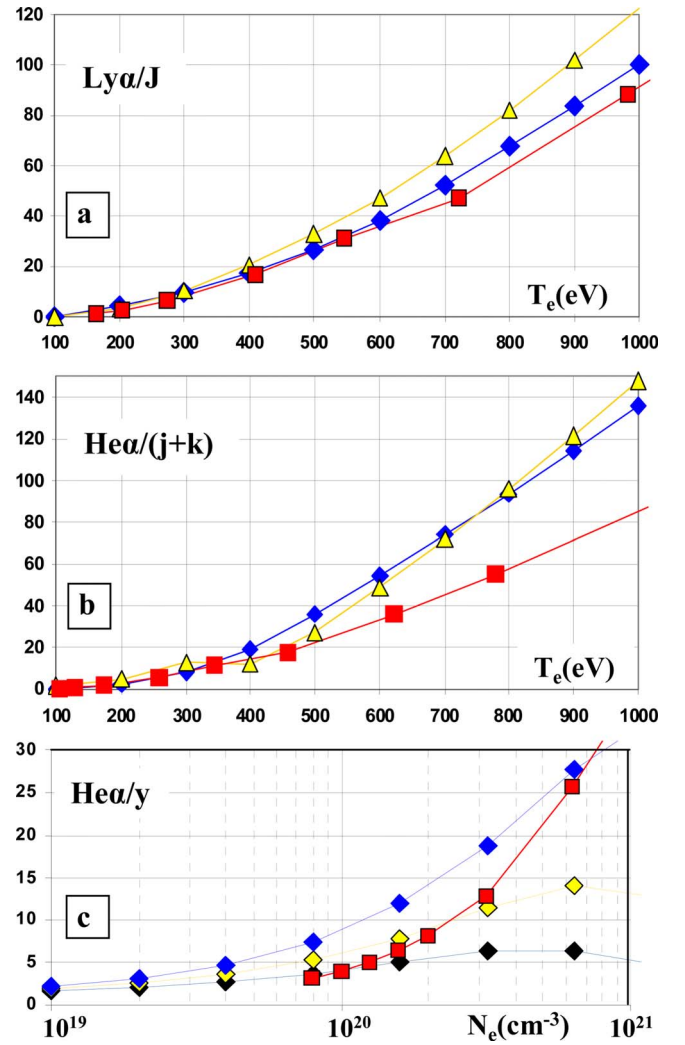


FIG. 16. (Color online) A comparison of the [(a) and (b)] electron temperature T_e and (c) density N_e calculated from the CE model (red squares), FLYCHK model [63] (blue diamonds), and PRISMPECT code [64] (yellow triangles) using the intensity ratio of (a) $\text{Ly}\alpha$ and [(b) and (c)] $\text{He}\alpha$ resonance lines to appropriate satellites. Lines in diagram (c) were calculated for $T_e = 200$ (black diamonds), 300 (yellow diamonds), and 400 eV (blue diamonds).

However, calculations [64] show that many of the aluminum satellite intensities are still close to their coronal values even at $N_e \sim 10^{20} \text{ cm}^{-3}$. A non-local thermodynamic equilibrium (LTE) collisional-radiative atomic kinetics model yields the CE model in the low-density limit. Thus, we compared the results of the CE model with those from collisional-radiative atomic kinetics models performed with the FLYCHK [65] and PRISMPECT [66] codes. Figure 16 compares calculations for the ratios of intensities of the resonance and appropriate satellite lines. Earlier it was noted that the Mg lines have small optical depth. Nevertheless, collisional-radiative calculations were done including the radiation transport effect both in the atomic kinetics level populations and in the line transport; the results are shown in Fig. 16. For example, and in our region of interest, the T_e and N_e deviations of the CE model from the FLYCHK model are 2%–3% for T_e [H], 10%–15% for T_e [He], and 30%–60% for N_e . Hence, the method of

satellite-to-resonance line ratios provides a reasonable estimation of T_e and N_e for plasmas in our time-integrated measurements.

IV. DISCUSSIONS

In this section the contribution of kinetic energy and Ohmic heating to the energy balance in wire-array Z pinches will be estimated for Zebra shots. The available kinetic energy and power of Spitzer plasma heating will be compared with the energy and power of x-ray pulses measured in experiments. Features of implosions and x-ray production in small-diameter wire arrays and possible mechanisms of plasma heating will be discussed.

A. Energy balance in wire arrays at the Zebra generator

The kinetic energy of imploding plasma can be calculated as the work done by the magnetic pressure [31],

$$K = \int \frac{B^2}{8\pi} 2\pi R l \left(\frac{-dR}{dt} \right) dt = \frac{a}{2} \Delta L I_0^2, \quad (3)$$

where K is the kinetic energy in kJ, I_0 is the peak current in MA, $\Delta L = 2l \ln(R_z/R_0)$ in nH, R_0 is the initial radius of the wire array, R_z is the radius of the stagnated Z pinch, l is the pinch length, and the coefficient a accounts for the current pulse shape. For Zebra implosions values $l=2$ cm, $I_0=1$ MA, and $R_z=0.45$ mm will be used. The parameter $a=0.68$ was calculated for the Zebra generator.

Contribution of the Ohmic plasma heating to the Z pinch energy and the power balance can be estimated using a Spitzer resistivity $\eta = 1.15 \times 10^{-14} \ln \Lambda Z(T_e)^{-3/2}$ s [67]. In Zebra implosions the electron plasma temperature is $T_e \sim 300\text{--}400$ eV, the ionization number in Al plasma is $Z \sim 12$, and the Coulomb logarithm is $\ln \Lambda \sim 6$. The depth of the skin layer is $\delta = (\nu_m t_{\text{stagn}})^{1/2}$, where t_{stagn} is the time of stagnation, $\nu_m = c^2/4\pi\sigma$ (cm²/s) is the magnetic diffusivity, and $\sigma = 1/\eta$ [31]. For typical stagnation time of ~ 20 ns the skin layer depth is $\delta = 0.15$ mm, and the power of Ohmic plasma heating with a Spitzer resistivity is $P_{Oh} = 80$ GW at the maximum of the current pulse. If we suggest the electron temperature of $T_e = 200$ eV then $P_{Oh} = 110$ GW. The Ohmic power is significantly less than the maximum power of the x-ray pulses radiated by Z pinches. If the current flows in the pinch volume due to mixing of the imploding plasma or mass transport [68] then the power of the Ohmic heating would be smaller unless the resistivity is non-Spitzer due to effects such as the Hall term or a longer current path in the structured plasma [32]. If a linear growth of the current density is suggested for implosion with strong mixing then integration gives the Ohmic power $P_{Oh} = 9\eta l^2 I / (8\pi R_z^2) = 16$ GW.

Using these estimates we can compare the kinetic energy and the energy of Spitzer Ohmic heating with the total radiated energy in Z pinches. Figure 10 presents x-ray pulses from cylindrical wire arrays with different diameters. The shaded areas show the part of the radiated x-ray energy which could be explained by dissipation of the kinetic energy. Based on the pinhole camera images we suggest a final

pinch diameter of 0.9 mm in these calculations. Below we estimate the impact of “necking” on the calculations of the kinetic energy. In the implosion of a 16 mm load, Fig. 10(a), the dissipation of the kinetic energy can produce the main x-ray pulse with the exception of the prepulse and the tail. In the 8 mm load, Fig. 10(b), the kinetic energy contributes $\sim 60\%$ to the energy of the main x-ray pulse. The contribution of the Ohmic heating in loads of 3–16 mm in diameter is much less than the contribution of the kinetic energy if we assumed, for estimation, a model of a uniform plasma column with a diameter of 0.9 mm and a length of 2 cm. Necks and hot spots were not included in the estimations because parameters of plasma are not clear in these areas.

The contribution of the kinetic energy decreases in the 2 mm load, Fig. 10(c), and almost disappears in the energy balance of 1 mm loads, Fig. 10(d). If we suggest that the final diameter of the pinch is equal to the diameter of the necks, 0.24 mm, then the calculated kinetic energy is ~ 0.45 kJ but the total radiated energy was ~ 10 kJ in this shot. The suggestion about the lack of kinetic energy is supported by the temporal dynamics of the x-ray pulse. Note that the neck diameter of 0.24 mm represents an upper bound for the size of the neck because of the spatial resolution of plasma diagnostics. The resolution of the laser shadowgraphy is $25 \mu\text{m}$ but the real diameter of the neck can be smaller if the dense neck is surrounded by a lower-density plasma, opaque at 532 nm. The spatial resolution of the x-ray pinhole camera is 0.25 mm. In Fig. 10(d) peaks on the x-ray pulse have $\sim 6\text{--}8$ ns rising edges. A rate of the power growth on the leading edge of the soft x-ray pulse, dP/dt , was calculated to find the signatures of different heating mechanisms. A value of the derivative dP/dt of the x-ray peaks is the same on the second x-ray peaks as in the first peak [see line 4 in Fig. 10(d)]. That could show that the kinetic energy does not prevail in the generation of the first peak.

Spitzer plasma heating in 1 mm loads is much smaller than the radiated power. In Fig. 10(d) the load produces the x-ray pulse at a current of ~ 0.5 MA. For this current the power of the Ohmic heating is ~ 20 GW [see line 3 in Fig. 10(d)]. Ohmic heating can produce a power of ~ 230 GW and explain the radiation presented in Fig. 10(d) if we suggest the radius of the homogeneous pinch $R_z = 0.1$ mm and $T_e = 300$ eV. The estimation for a Spitzer heating in necks gives a higher level of power than the homogeneous pinch but the parameters of plasma are unknown in these areas. The energy balance in 1 mm wire arrays can be linked to necks, bright spots, and other physical mechanisms [30–32]. Note that the calculated pinch resistivity could be different due to plasma nonuniformity. The mechanism of the heating provides a fast rising edge of the x-ray pulse with a power of up to 0.25 TW and energy of 1–2 kJ in the single burst.

The rate of the power growth on the leading edge of the soft x-ray pulse dP/dt was calculated. Figure 17 presents a correlation of dP/dt and peak power P in 3 mm 16-wire arrays. This leads to the suggestion that the radiated x-ray power is higher if the rate of the plasma heating is faster.

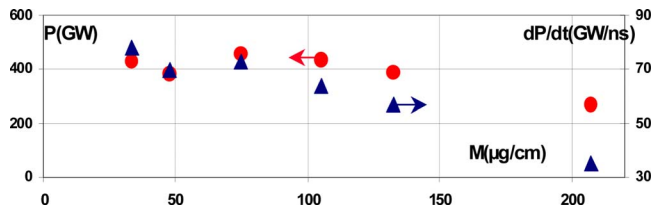


FIG. 17. (Color online) The correlation between the maximum x-ray power P and the maximum rate of power, dP/dt , on the leading edge of the x-ray pulse in Al of 3 mm loads with different masses.

B. Features of implosions and x-ray production in small-diameter wire arrays

Several physical mechanisms were suggested to explain the enhanced energy dissipation in Z pinches but experiments have thus far not been able to conclusively distinguish between these mechanisms. This study of small-diameter wire arrays with small kinetic energy shows features of non-kinetic-energy dissipation. The ablation rate is faster in small-diameter loads than in arrays of 12–16 mm in diameter, and plasma accumulates faster in the inner volume. The current flowing in plasma could be a driving force for instabilities at the ablation phase. A bubblelike implosion delivers material and the main current to the center of the array and forms a pinch with necks. The main x-ray pulse starts 3–5 ns after the bubblelike implosion. In 1–2 mm wire arrays the nonkinetic heating mechanism generates the x-ray pulse with a fast 6–8 ns rising edge and power of 0.25–0.35 TW. The multi-peaks temporal structure of x-ray pulses in 1 mm arrays reflects the dynamics of plasma heating. The energy radiated in a single peak of the multi-peak x-ray pulse is 1–2 kJ. The x-ray energy and power radiated in both soft and keV ranges

fall in loads 1–2 mm in diameter. The electron temperature T_e in Z pinches also tends to decrease in loads 1 mm in diameter.

Bright radiating spots are seen in x-ray images of the pinch. Following the observations of implosions in small-diameter loads, we could suggest that the energy dissipation is linked to the formation of necks in the Z pinch. Bubblelike implosion with correlated bubbles snowplows the material and switches the current to the central pinch. The kinetic energy is focused in small areas with a final diameter of <0.3 mm. The location of necks correlates to long-lived bright spots rising in the beginning of the main x-ray pulse. The short-lived bright spots generate short powerful bursts on the x-ray pulse and could be produced by another physical mechanism. Bright spots could be linked to the MHD instability, radiative collapse, disruption on the pinch, or cells of flute-mode instability [36,53–55]. There are multiple plausible scenarios that could explain the experimental data. The identification of nonkinetic plasma heating needs the development of diagnostics with high spatial, temporal, and spectral resolutions. Small-diameter wire arrays with small kinetic energy of implosion are good objects to study the mechanisms of energy dissipation in Z pinches. Further experiments with high-resolution x-ray and ultraviolet probing diagnostics are scheduled to clarify the origin, the dynamics, and the role of nonkinetic heating in wire-array Z pinches.

ACKNOWLEDGMENTS

The authors thank B. Jones for reading the paper and useful comments. The authors also thank R. Presura, B. Le-Galloudec, V. Nalajala, S. Batie, T. J. Adkins, and D. Macaulay for help. This work was supported by the DOE/NNSA under UNR Grant No. DE-FC52-06NA27616.

-
- [1] T. W. L. Sanford *et al.*, Phys. Rev. Lett. **77**, 5063 (1996).
 - [2] C. Deeney, M. R. Douglas, R. B. Spielman, T. J. Nash, D. L. Peterson, P. L'Éplattenier, G. A. Chandler, J. F. Seamen, and K. W. Struve, Phys. Rev. Lett. **81**, 4883 (1998).
 - [3] R. B. Spielman *et al.*, Phys. Plasmas **5**, 2105 (1998).
 - [4] M. E. Cuneo *et al.*, Phys. Rev. E **71**, 046406 (2005).
 - [5] W. A. Stygar *et al.*, Phys. Rev. E **69**, 046403 (2004).
 - [6] D. D. Ryutov, M. S. Derzon, and M. K. Matzen, Rev. Mod. Phys. **72**, 167 (2000).
 - [7] M. K. Matzen *et al.*, Phys. Plasmas **12**, 055503 (2005).
 - [8] W. A. Stygar *et al.*, Phys. Rev. E **72**, 026404 (2005).
 - [9] S. V. Lebedev, I. H. Mitchell, R. Aliaga-Rossel, S. N. Bland, J. P. Chittenden, A. E. Dangor, and M. G. Haines, Phys. Rev. Lett. **81**, 4152 (1998).
 - [10] S. C. Bott *et al.*, Phys. Rev. E **74**, 046403 (2006).
 - [11] V. V. Alexandrov *et al.*, J. Exp. Theor. Phys. **97**, 745 (2003).
 - [12] B. Jones *et al.*, Phys. Rev. Lett. **95**, 225001 (2005).
 - [13] B. Jones *et al.*, Phys. Plasmas **13**, 056313 (2006).
 - [14] V. V. Ivanov *et al.*, Phys. Rev. Lett. **97**, 125001 (2006).
 - [15] S. V. Lebedev *et al.*, Plasma Phys. Controlled Fusion **47**, A91 (2005).
 - [16] G. S. Sarkisov, P. V. Sasorov, K. W. Struve, D. H. McDaniel, A. N. Gribov, and G. M. Oleinik, Phys. Rev. E **66**, 046413 (2002).
 - [17] D. B. Sinars, M. E. Cuneo, E. P. Yu, D. E. Bliss, T. J. Nash, J. L. Porter, C. Deeney, M. G. Mazarakis, G. S. Sarkisov, and D. F. Wenger, Phys. Rev. Lett. **93**, 145002 (2004).
 - [18] V. V. Ivanov, V. I. Sotnikov, A. Haboub, A. P. Shevelko, A. L. Astanovitskiy, A. Morozov, E. D. Kazakov, and S. D. Altemara, Phys. Rev. Lett. **100**, 025004 (2008); V. V. Ivanov *et al.*, 2007 Wire Array Workshop, Battle, England, UK (unpublished).
 - [19] V. V. Ivanov *et al.*, Phys. Plasmas **14**, 032703 (2007).
 - [20] H. Sze, J. Banister, B. H. Failor, J. S. Levine, N. Qi, A. L. Velikovich, J. Davis, D. Lojewski, and P. Sincerny, Phys. Rev. Lett. **95**, 105001 (2005).
 - [21] C. Deeney, T. Nash, P. D. LePell, K. Childers, and M. Krishnan, J. Quant. Spectrosc. Radiat. Transf. **44**, 457 (1990).
 - [22] C. Deeney *et al.*, Phys. Plasmas **5**, 2431 (1998).
 - [23] C. Deeney *et al.*, Phys. Rev. E **56**, 5945 (1997).
 - [24] C. Deeney, T. Nash, R. R. Prasad, L. Warren, K. G. Whitney, J. W. Thornhill, and M. C. Coulter, Phys. Rev. A **44**, 6762

- (1991).
- [25] J. W. Thornhill, K. G. Whitney, C. Deeney, and P. D. LePell, *Phys. Plasmas* **1**, 321 (1994).
- [26] D. L. Peterson *et al.*, *Phys. Plasmas* **5**, 3302 (1998).
- [27] K. G. Whitney *et al.*, *Phys. Plasmas* **11**, 3700 (2004).
- [28] R. H. Lovberg, R. A. Riley, and J. S. Shlachter, in *Proceedings of the 3rd International Conference on Dense Z Pinches*, AIP Conf. Proc. Vol. 299, London, UK (Springer, New York, 1993), pp. 59–68.
- [29] R. Riley, D. Scudder, J. Shlachter, and R. Lovberg, *Phys. Plasmas* **3**, 1314 (1996).
- [30] L. I. Rudakov, A. L. Velikovich, J. Davis, J. W. Thornhill, J. L. Giuliani, and C. Deeney, *Phys. Rev. Lett.* **84**, 3326 (2000).
- [31] A. L. Velikovich *et al.*, *Phys. Plasmas* **7**, 3265 (2000).
- [32] V. L. Kantsyrev *et al.*, *IEEE Trans. Plasma Sci.* **34**, 2295 (2006).
- [33] V. L. Kantsyrev *et al.*, *High Energy Density Phys.* **3**, 136 (2007).
- [34] M. G. Haines, P. D. LePell, C. A. Coverdale, B. Jones, C. Deeney, and J. P. Apruzese, *Phys. Rev. Lett.* **96**, 075003 (2006).
- [35] J. P. Chittenden, S. V. Lebedev, C. A. Jennings, S. N. Bland, and A. Ciardi, *Plasma Phys. Controlled Fusion* **46**, B457 (2004).
- [36] V. I. Sotnikov *et al.*, *IEEE Trans. Plasma Sci.* **34**, 2239 (2006).
- [37] F. Winterberg, *Z. Naturforsch., A: Phys. Sci.* **63a**, 35 (2008).
- [38] V. V. Ivanov *et al.*, *IEEE Trans. Plasma Sci.* **35**, 1170 (2007).
- [39] D. Sinars *et al.*, *Phys. Rev. Lett.* **100**, 145002 (2008).
- [40] C. A. Coverdale, C. Deeney, M. R. Douglas, J. P. Apruzese, K. G. Whitney, J. W. Thornhill, and J. Davis, *Phys. Rev. Lett.* **88**, 065001 (2002).
- [41] C. A. Coverdale *et al.*, *Phys. Plasmas* **15**, 023107 (2008).
- [42] C. A. Coverdale *et al.*, *IEEE Trans. Plasma Sci.* **35**, 582 (2007).
- [43] B. S. Bauer *et al.*, in *Proceedings of the 4th International Conference on Dense Z-Pinches* (Springer, New York, 1997), p. 153.
- [44] R. Presura (private communication).
- [45] V. V. Ivanov *et al.*, *IEEE Trans. Plasma Sci.* **34**, 2247 (2006).
- [46] V. V. Ivanov *et al.*, *Phys. Plasmas* **13**, 012704 (2006).
- [47] S. V. Lebedev *et al.*, *Phys. Plasmas* **8**, 3734 (2001).
- [48] S. E. Lebedev *et al.*, *Laser Part. Beams* **19**, 355 (2001).
- [49] J. P. Chittenden *et al.*, *Phys. Rev. E* **61**, 4370 (2000).
- [50] P. G. Burkhalter, C. M. Dozier, and D. J. Nagel, *Phys. Rev. A* **15**, 700 (1977).
- [51] D. H. Kalantar and D. A. Hammer, *Phys. Rev. Lett.* **71**, 3806 (1993).
- [52] G. N. Hall *et al.*, *Phys. Plasmas* **13**, 082701 (2006).
- [53] K. N. Koshelev and N. R. Pereira, *J. Appl. Phys.* **69**, R21 (1991).
- [54] S. A. Pikuz *et al.*, *J. Quant. Spectrosc. Radiat. Transf.* **71**, 581 (2001).
- [55] C. Deeney *et al.*, *AIP Conf. Proc.* **195**, 62 (1989).
- [56] T. Nash *et al.*, *Rev. Sci. Instrum.* **70**, 302 (1999).
- [57] F. J. Marshall, J. P. Knauer, D. Anderson, and B. L. Schmitt, *Rev. Sci. Instrum.* **77**, 10F308 (2006); K. M. Chandler *et al.*, *ibid.* **76**, 113111 (2005).
- [58] H. R. Griem, *Principles of Plasma Spectroscopy* (Cambridge University Press, New York, 1997).
- [59] L. A. Vainshtein, U. I. Safronova, and A. M. Urnov, in *Dielectronic Satellites of Resonance Lines of Highly Charged Ions*, Proceedings of the Lebedev Physical Institute, edited by N. G. Basov (Nova Science, Commack, NY, 1980), Vol. 119, p. 13.
- [60] V. Vinogradov, *et al.*, *Sov. J. Quantum Electron.* **5**, 630 (1975).
- [61] L. P. Presnyakov, *Sov. Phys. Usp.* **19**, 387 (1976).
- [62] A. H. Gabriel, *Mon. Not. R. Astron. Soc.* **160**, 79 (1972).
- [63] B. Jones *et al.*, *J. Quant. Spectrosc. Radiat. Transf.* **99**, 341 (2006).
- [64] D. Duston, J. E. Rogerson, J. Davis, and M. Blaha, *Phys. Rev. A* **28**, 2968 (1983).
- [65] H. K. Chung *et al.*, *High Energy Density Phys.* **1**, 3 (2005).
- [66] J. J. MacFarlane, I. E. Golovkin, P. Wang, P. R. Woodruff, and N. A. Pereyra, *High Energy Density Phys.* **3**, 181 (2007).
- [67] J. D. Huba, *NRL Plasma Formulary* (Naval Research Laboratory, Washington, DC, 1998).
- [68] B. Jones *et al.*, *Phys. Rev. Lett.* **100**, 105003 (2008).